Evaluating f-orbital Participation in the U^{V}=E Multiple Bonds of $[U(E)(NR_2)_3]$ (E = O, $NSiMe_3$, NAd; R =$SiMe_3$)

Thien H. Nguyen,[a] *Edward L. Paul,*[a] *Wayne W. Lukens,**[b] *and Trevor W. Hayton**[a]

[a] Department of Chemistry and Biochemistry, University of California, Santa Barbara, Santa Barbara, California 93106, USA

[b] Chemical Sciences Division, Lawrence Berkeley National Laboratory, Berkeley, California, 94720, USA

[†] Corresponding Authors: hayton@chem.ucsb.edu, wwlukens@lbl.gov

Abstract

The reaction of 1 equiv of 1-azidoadamantane with $[U^{III}(NR_2)_3]$ (R = $SiMe_3$) in Et_2O results in formation of $[U^{V}(NR_2)_3(NAd)]$ (**1**, Ad = 1-adamantyl) in good yields. The electronic structure of **1**, as well as those of the related U(V) complexes, $[U^{V}(NR_2)_3(NR)]$ (**2**) and $[U^{V}(NR_2)_3(O)]$ (**3**), were analyzed with EPR spectroscopy, SQUID magnetometry, NIR-visible spectroscopy, and crystal field modeling. This analysis revealed that, within this series of complexes, the steric bulk of the E^{2-} (E = O, NR) ligand is the most important factor in determining the electronic structure. In particular, the increasing steric bulk of this ligand, on moving from O^{2-} to $[NAd]^{2-}$, results in increasing U=E distances and E-U-N_{amide} angles. These changes have two principal effects on the resulting electronic structure: (1) the increasing U=E distances decreases the energy of the f_σ orbital, which is primarily σ^* with respect to the U=E bond, and (2) the increasing E-U-N_{amide} angles increases the energy of f_δ, due to increasing anti-bonding interactions with the amide ligands. As a result of the latter change, the electronic ground state for complexes **1** and **2** is primarily f_φ in character, whereas the ground state for complex **3** is primarily f_δ.

Introduction

Actinide-ligand covalency has been studied using a variety of experimental techniques, including X-ray absorption spectroscopy,[1-8] X-ray crystallography,[9-12] NMR spectroscopy,[13-25] EPR spectroscopy,[26-29] and optical spectroscopy.[30-32] With respect to optical spectroscopy, complexes with the $5f^1$ electronic configuration have proven to be especially useful.[30, 33-36] The lack of electron-electron repulsion in this configuration allows the spin-orbit coupling to be treated in a relatively straight-forward manner.[31, 32] For example, in 2013 we reported a comprehensive bonding analysis of a series of O_h-symmetric $5f^1$ complexes, including $[U^V(CH_2SiMe_3)_6]^-$, $[U^V(O^tBu)_6]^-$, and $[U^VX_6]^-$ (X = F, Cl, Br),[31] which permitted an estimate of the strengths of the ligand-f-orbital interactions. More recently, Liddle and co-workers analyzed the optical and EPR spectra of the C_{3v}-symmetric U(V) nitride, $[U^V(Tren^{TIPS})(N)]^-$ ($Tren^{TIPS}$ = $N(CH_2CH_2NSi^iPr_3)_3$), and extracted the corresponding crystal field splitting parameters.[37] We subsequently performed a similar analysis on the bridged-nitride complex, $[(NR_2)_3U^V(\mu\text{-}N)Th^{IV}(NR_2)_3]$ (R = $SiMe_3$), which also features C_{3v}-symmetry.[38] These studies demonstrated that, for both complexes, the U-$N_{nitride}$ interaction strongly destabilizes the f_σ orbital and (to a lesser extent) the f_π orbitals. These two studies are also notable because they demonstrate that a detailed crystal field analysis can be successfully performed on symmetries lower than O_h, which significantly expands the range of compounds that can be interrogated by this method.

Herein, we report the synthesis of the U(V) 1-adamantylimido complex, $[U^V(NR_2)_3(NAd)]$ (**1**, R = $SiMe_3$), along with a detailed analysis of its U=N bonding. For comparison, we performed spectroscopic analyses on the previously reported U(V) imido complex, $[U^{V}(NR_2)_3(NR)]$ (**2**), and U(V) oxo complex, $[U^{V}(NR_2)_3(O)]$ (**3**).[39, 40] Our analysis shows that the electronic structures of these complexes are largely dictated by the U=E interaction. Moreover, the differences in their electronic structures are attributable to changes in the steric bulk of the E^{2-} (E = O, NR) ligand, which affects both the metal-ligand bond lengths and the inter-ligand angles.

Results and Discussion

Synthesis. Addition of 1 equiv of 1-azidoadamantane to $[U^{III}(NR_2)_3]$ (R = $SiMe_3$) in diethyl ether results in the formation of dark green solution concomitant with the evolution of gas. From this solution, $[U^{V}(NR_2)_3(NAd)]$ (**1**, Ad = 1-adamantyl) can be isolated in 56% yield as green needles after work-up (Scheme 1). The ^1H NMR spectrum of **1** in C_6D_6 exhibits a broad resonance at -3.92 ppm, which is assignable to the 54 protons of the NR_2 ligands. It also exhibits resonances at 8.45, 10.53, 16.72, and 20.02 ppm, in a 3:3:3:6 ratio, which are assignable to the four expected proton environments of the 1-adamantyl imide ligand.

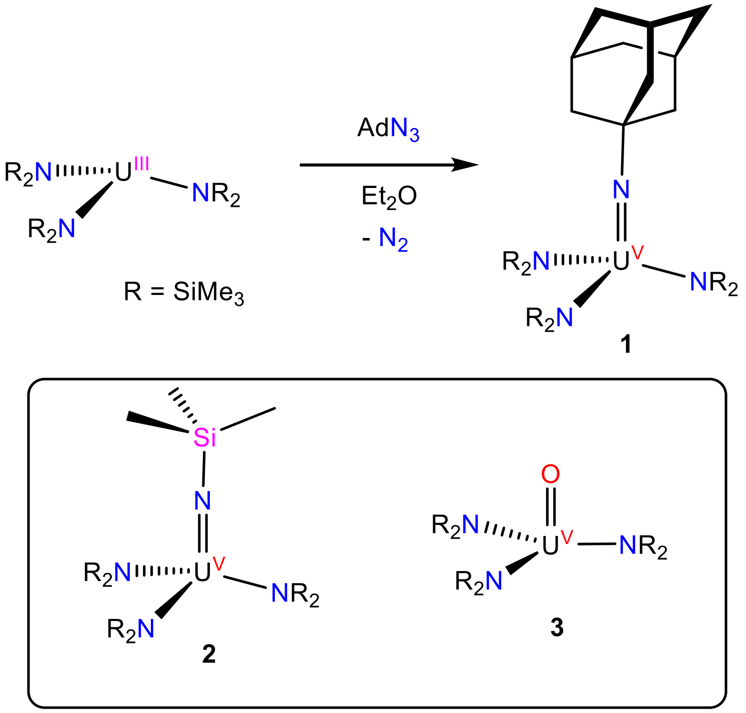

Scheme 1. Synthesis of complex **1**. Inset: molecular structures of **2** and **3**.

Storage of a concentrated solution of **1** in diethyl ether at -25 °C for 24 h results in the formation of crystals suitable for X-ray analysis. Complex **1** crystalizes in the triclinic space group P-1, and its solid state molecular structure is shown in Figure 1. In the solid state, **1** adopts a pseudotetrahedral geometry about the U(V) center. The U-N_{imido} distance is 1.945(2) Å and the U-N-C angle is 178.8(2)° (Table 1). These parameters are similar to those reported for other U(V) mono(imido) complexes.[41-45] For example, $[U^V(NR_2)_3(NSiMe_3)]$ features a U-N_{imido} distance of 1.910(6) Å and a similar U-N-C angle.[39] The U-N_{amide} distances in **1** range from 2.269(2) to 2.272(2) Å, which are comparable to those reported for other $[U^V(NR_2)_3(E)]$-type complexes (Table 1). The N_{amide}-U-N_{imide} angles exhibit a remarkably large range, from 99.12(9) to 123.46(9), which is likely a consequence of steric pressure from the adamantyl group. A structural comparison of **1** vs. **3** is also informative. In particular, the structure of **3**, e.g.,

[$U^V(NR_2)_3(O)$], is trigonal pyramidal, wherein the U atom is almost in the plane defined by the three N atoms of the NR_2 ligands. This difference is most clearly seen in the average E-U-N_{amide} angles, which is 93° for **3** vs. 111° for **1**. The N_{amide}-U-E angle of **2** (103°) is intermediate between those of pseudotetrahedral **1** and trigonal pyramidal **3**.

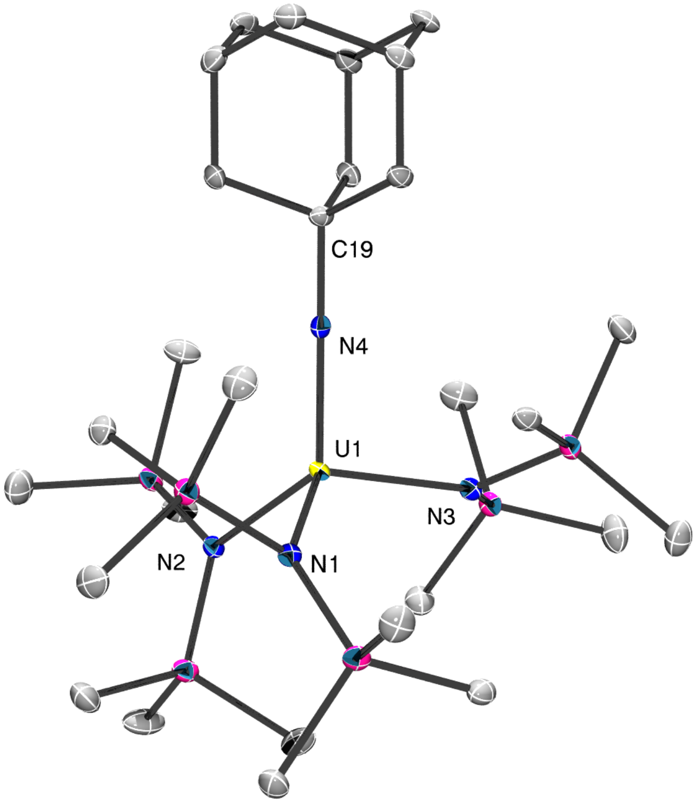

Figure 1. ORTEP diagram of [$U^V(NR_2)_3(NAd)$] (**1**) with 50% probability ellipsoids. H atoms omitted for clarity.

Table 1. Selected metrical parameters of **1**, [$U^V(NR_2)_3(NSiMe_3)$] (**2**), [$U^V(NR_2)_3(O)$] (**3**), [$U^V(NR_2)_3(NCPh_3)$], and [$Na(12\text{-crown-}4)_2$][$U^V(Tren^{TIPS})(N)$].[39, 40, 43, 46] Space-filling diagrams of **3** and [$Na(12\text{-crown-}4)_2$][$U^V(Tren^{TIPS})(N)$], which illustrate the different steric profiles of the NR_2 and $Tren^{TIPS}$ ligand sets, can be found in the Supporting Information (Figure S5).

Parameters	**1**	**2**	**3**	**[U^{V}(NR$_2$)$_3$(NCPh$_3$)]**	**[Na(12-crown-4)$_2$][U^{V}(Tren^{TIPS})(N)]**
U=E (Å)	1.945(2)	1.910(6)	1.817(1)	1.959(5)	1.83(2)
U-NR$_2$ (Å)	2.269(2), 2.270(2), 2.272(2)	2.29(1)	2.235(1), 2.244(2), 2.242(1)	2.264(3)	2.33(2) 2.37(2) 2.37(1)
N-U-E (°)	110.59(9), 123.46(9), 99.12(9) 111.1 (av.)	103(2)	92.53(6), 92.16(6), 92.48(5) 92.4 (av.)	113.90(7)	107.9(10) 115.1(6) 112.0(7) 110.5 (av.)
N-U-N (°)	101.23(8) 116.38(8) 106.96(9)	115(2)	119.30(5), 118.16(5), 122.02(5)	104.70(8)	108.0(5) 107.2(5) 110.1(5)
U-N-C (°)	178.8(2)	180	-	180	--

Electronic structure of pentavalent [U^{V}(E)(NR$_2$)$_3$] complexes in D_{3h} symmetry. The splitting of the 5f^1 states in complexes with strongly bound axial ligands has been investigated for [Np^{VI}O$_2$]$^{2+}$,[35, 36, 47, 48] [U^{V}(Tren^{TIPS})(N)]$^{-}$,[37] and [(NR$_2$)$_3$U^{V}(μ-N)Th^{IV}(NR$_2$)$_3$][38]. The electronic structure of [U^{V}(Tren^{TIPS})(N)]$^{-}$ has been studied in detail by both *ab initio* calculations and crystal field modeling. It has a high-lying 5f excited state at ~18000 cm^{-1} largely due to the U-N σ* interaction. In addition, the complex has a ground state with $m_j = \pm 5/2$ and a low-lying excited state with $m_j = \pm 3/2$, which is around 300 cm^{-1} higher in energy. The results of the *ab initio* calculations were in good agreement with the energies of the 5f-5f transitions observed in the NIR. The other notable study is that performed on [Np^{VI}O$_2$]$^{2+}$ by Eisenstein and Pryce, who used crystal field theory to explain the electronic structure and optical spectrum of the neptunyl ion.[35] We can use the same approach, in combination with the results of the *ab initio* calculations on $[U^V(Tren^{TIPS})(N)]^-$, to describe how the crystal field and spin orbit coupling (SOC) result in the electronic structures of **1-3** and $[U^V(Tren^{TIPS})(N)]^-$. Following the approach used by Eisenstein and Pryce, the states are represented as $|m_l\ m_s\rangle$ where m_s is + or – to represent +1/2 and -1/2.[35] In D_{3h} symmetry, the $5f^1$ states consist of seven Kramers doublets, which are pairs of states with opposite signs of m_l and m_s, e.g., $|1+\rangle$ and $|\text{-}1\text{-}\rangle$. For brevity, only the component of the Kramers doublet with $m_l \geq 0$ are shown in Figure 2 and discussed in the text. To better visualize how the crystal field and spin orbit coupling (SOC) affect the NIR spectra of these complexes and to generate starting values for these parameters, the splitting of the 5f states can be expressed to zeroth-order (parameters only affect the energies of the states and do not mix the states) in D_{3h} symmetry. The zeroth-order splitting of the states is shown in Figure 2 and is based on the assumptions that the crystal field of the oxo or imido ligand is larger than the spin orbit coupling (SOC), and that SOC is slightly larger than the crystal field splitting due to the three NR_2 ligands. This scheme was used by Eisenstein and Pryce to investigate the electronic structure of $Np^{VI}O_2^{2+}$.[35] At the left, the energies of the states are shown without SOC and assuming axial symmetry. The initial ordering reflects the presence of both the strongly bound oxo or imido ligand and the more weakly bound NR_2 ligands, and the ordering is largely based on the *ab initio* calculations of the states found in $[U^V(Tren^{TIPS})(N)]^-$ in the absence of SOC.[37] Therefore, the energy of f_φ, E_3, is greater than that of f_δ, E_2, because the NR_2 ligands lie close the XY plane, especially in **3**. The effect of SOC is shown in the middle of Figure 2; SOC splits the $5f^1$ states into seven

Kramers doublets. Finally, the right side of Figure 2 shows the effect of reducing the symmetry from axial to D_{3h}, which mixes the |3+⟩ and |3-⟩ states.

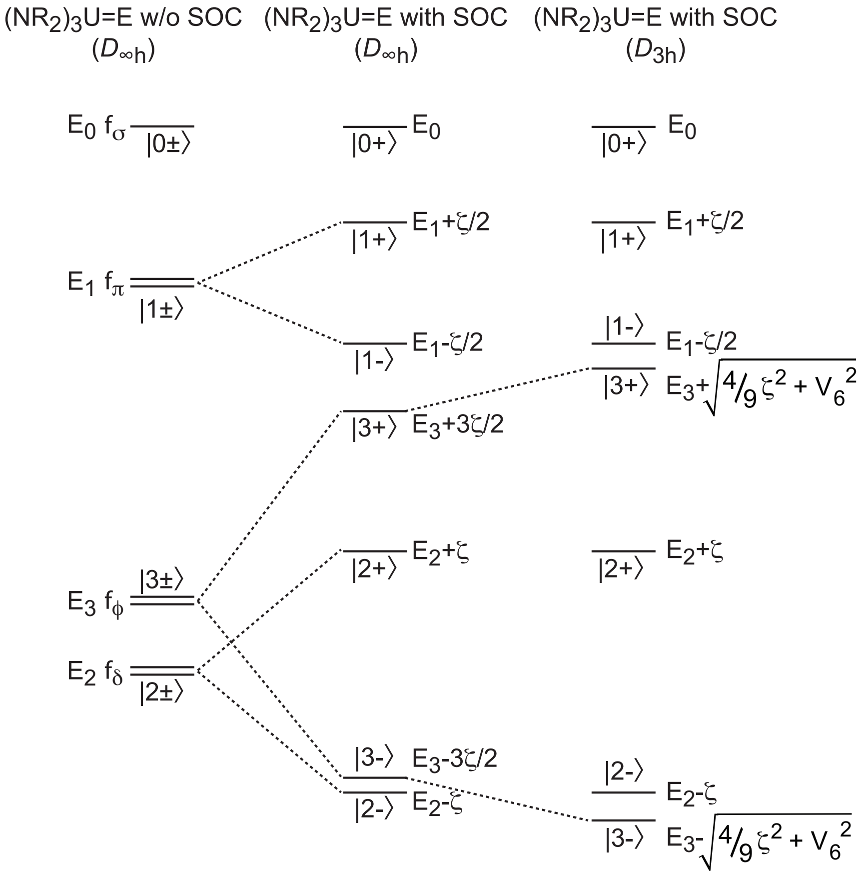

Figure 2. Zeroth-order splitting of the $5f^1$ states of $[U^V(E)(NR_2)_3]$ complexes (not to scale). Horizontal lines correspond to Kramers doublets of which only the component with $m_l \geq 0$ is shown. The states are shown as $|m_l\, m_s\rangle$ where m_s is indicated by + or -.

In D_{3h} symmetry, the highest energy 5f state is |0+⟩, which is U=E σ antibonding. The next three states are |1+⟩ and |1-⟩, which are U=E π antibonding, followed by |3+⟩, which is U-NR$_2$ σ antibonding if the -NR$_2$ ligands lie in the XY plane. The relative energies of |1-⟩ and |3+⟩ depend on the values of E_1 and E_3. The final three states, |2+⟩, |2-⟩, and |3-⟩

are weakly U-NR_2 antibonding. The lowest energy states are |3-⟩ and |2-⟩, and the identity of the ground state depends on the strength of the U-NR_2 interaction, as well as the geometry of the complex. As shown previously, the ground state in pseudotetrahedral complexes is |3-⟩,[35-38] but E_3 increases relative to E_2 as the complex adopts a geometry closer to trigonal pyramidal, as in **3**. As a result, the calculated ground states of **3** and [U^V(O)(Tren^{TIPS})] are |2-⟩, likely due to their deviations from pseudotetrahedral symmetry.[37, 40]

Electron paramagnetic resonance (EPR) spectroscopy. EPR spectroscopy provides information about the nature of the ground state, which can be used to assign $|m_l\ m_s\rangle$. In particular, the $g_{||}$ values of |3-⟩ and |2-⟩ are 4 and 2, respectively, whereas $g_\perp$ is zero in both cases.[49] The crystal field and spin orbit coupling will alter these values, but the observed EPR transition is likely due to $g_{||}$ because $g_\perp$ is small unless there is a large degree of mixing among the states. The EPR spectrum of **3** (recorded at 3K) consists of a single peak with g = 2.17, which suggests a |2-⟩ ground state.[40] The EPR spectra of **1** and **2** at 3K are shown in Figure S3. In **1**, $g_{||}$ is 3.60, which is consistent with a |3-⟩ ground state. For **2**, $g_{||}$ is 2.50 for **2**, which is consistent with either |3-⟩ or |2-⟩ as the ground state. The other features in the spectra are due to crystallites from incomplete powder averaging. Their presence indicates that the resonance field for $g_\perp$ is larger than 1 T; thus, $g_\perp$ is less than 0.7 for complexes **1-3** (and outside of the range of the spectrometer).

Near-Infrared spectroscopy. The Vis-NIR spectra of **1-3** were recorded in toluene and modeled using pseudoVoigt peaks (Figures 3-5). The positions of the peaks are given in

Table 2. In all spectra, the |0+⟩ peak can be identified as the intense peak (relative to the other 5f-5f transitions) on the shoulder of a much more intense peak at higher energy. The much greater intensity of the |0+⟩ peak relative to the other 5f-5f peaks is consistent with greater orbital mixing between the U $5f_{\sigma}$ and E $2p_z$ orbitals relative to the other interactions (due to "intensity stealing," which relaxes the selection rule for the symmetry forbidden 5f-5f transitions), which is in turn consistent with the short U=E distances observed in these compounds.[50] The total number of peaks observed in the NIR region is six for **1** and **2** and five for **3**. The spectra of **1** and **2** are similar in that each has a strong |0+⟩ peak above 15000 cm^{-1} followed by two sets of two peaks that are close together in energy. The spectrum of **3** is somewhat different. While it too has a strong |0+⟩ peak, the other peaks are well separated in energy.

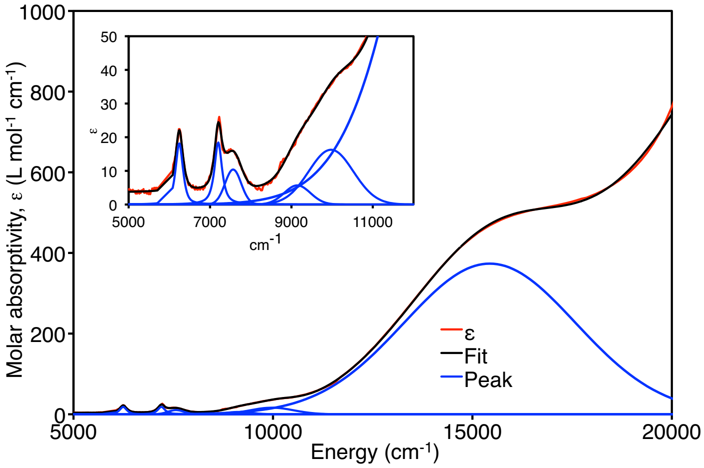

Figure 3. Room temperature Vis-NIR absorption spectrum for **1** (0.52 mM, C_7H_8). Inset shows magnified NIR spectrum.

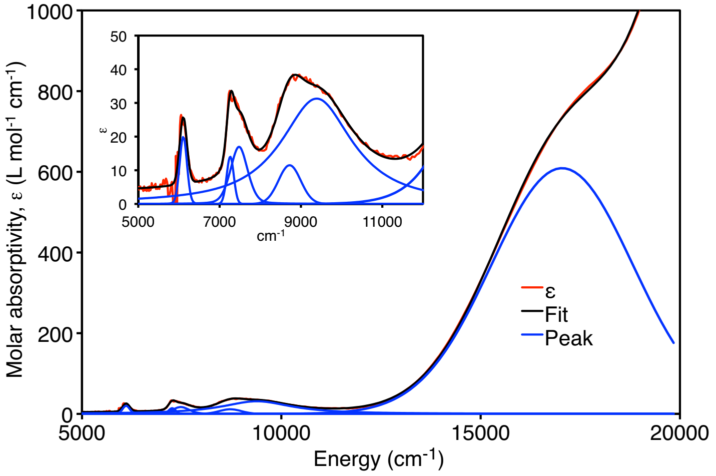

Figure 4. Room temperature Vis-NIR absorption spectrum for **2** (0.52 mM, C_7D_8). Inset shows magnified NIR spectrum.

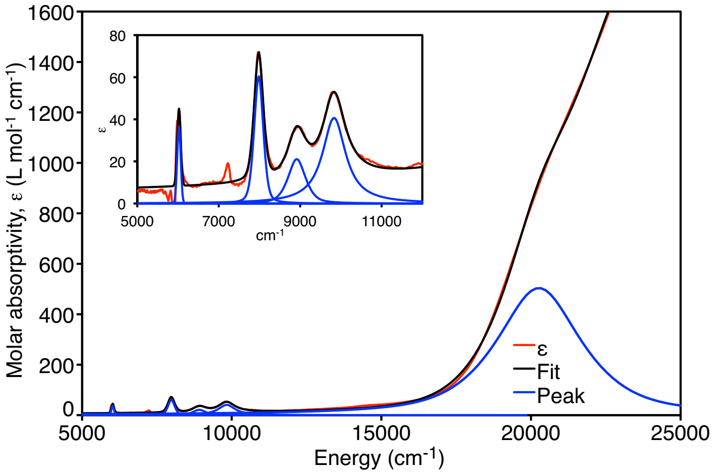

Figure 5. Room temperature Vis-NIR absorption spectrum for **3** (0.54 mM, C_7D_8). Inset shows magnified NIR spectrum.

Magnetic susceptibility. Variable temperature magnetic susceptibility of **1** and **2** were measured and are shown in Figure 6 along with the magnetic susceptibility data previously reported for **3**.[40] The effective magnetic moment of **1** is 2.47 μ_B at 300 K, whereas complex **2** has an effective magnetic moment of 2.12 μ_B at 300 K. These values are comparable to the moments reported for other U(V) complexes.[41, 51, 52] Complex **3** exhibits a much lower effective magnetic moment of 1.59 μ_B at room temperature.[40] This value is comparable to that of the U(V) terminal oxo complex reported by Liddle, $[U^V(O)(Tren^{TIPS})]$, which is 1.79 μ_B at 300 K.[53] The plot of χT vs T for **2** shows a distinct change in slope on traversing from 70 to 100 K, which indicates that an excited state becomes populated at these temperatures. The population of an excited Kramers doublet is ~5% when the thermal energy is 1/3 of the energy of the state, which is often sufficient to see a change in the slope of the χT vs T plot. For both **1** and **3**, the plots of χT vs T are roughly linear, which means that either (1) only the ground state is thermally populated to 300 K, or (2) the magnetic moment of the excited state is sufficiently similar to that of the ground state that it does not change the slope of χT vs T. An example of the latter effect is seen in the magnetic susceptibility of PuO_2, which is linear from 0 K to 1000 K even though exited states become thermally populated.[54, 55]

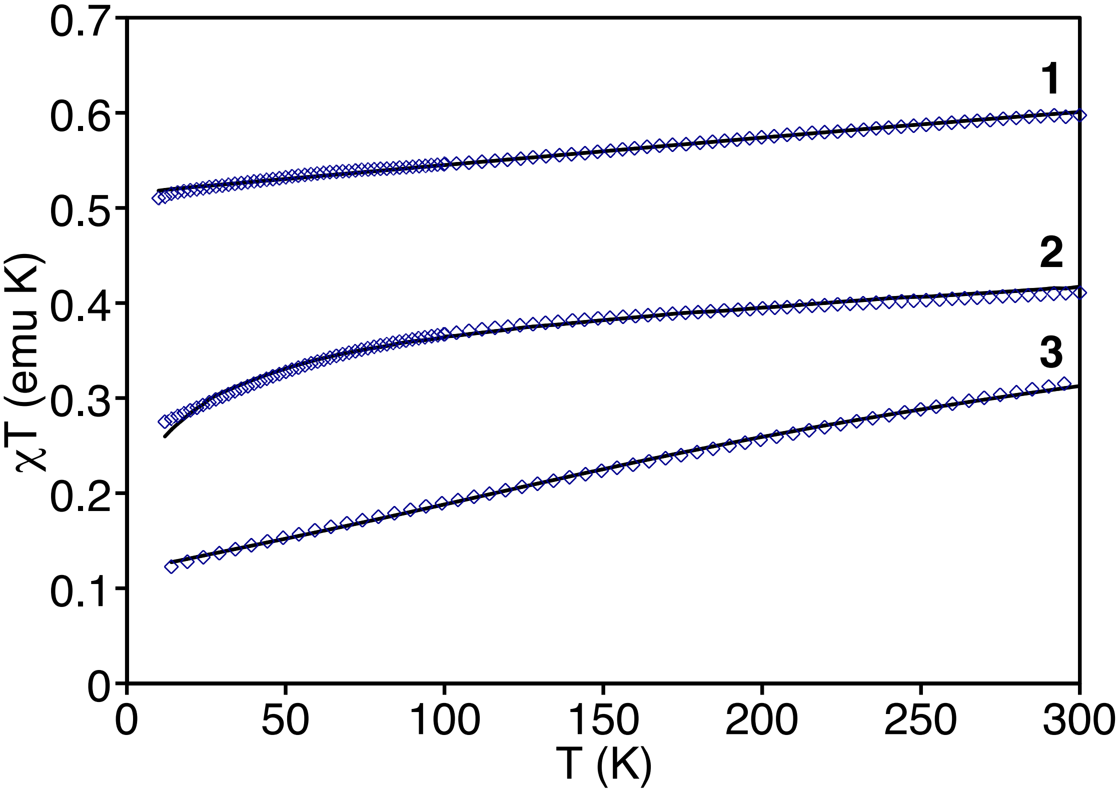

Figure 6. Magnetic susceptibility (as χT) of complexes **1-3**. Data are shown as open blue symbols, fits to the data are shown as solid black lines.

Crystal field modeling. The magnetic susceptibilities of **1-3** from 10 to 300 K, and the energies of the peaks observed in the NIR spectra, were modeled by crystal field theory using the program CONDON 3.0.[56] Data were modeled in both C_{3v} and D_{3h} symmetry. The differences between these two symmetries are that, in C_{3v} symmetry, states with m_j that the differ by ±3 may mix with each other, whereas in D_{3h} symmetry, only states with m_j that the differ by ±6 may mix, where $m_j = m_l + m_s$. Likewise, in C_{3v} symmetry, orbitals with m_l that the differ by ±3 may mix, whereas in D_{3h} symmetry, only orbitals with m_l that the differ by ±6 may mix. In addition, C_{3v} symmetry requires 6 parameters to describe the crystal field, whereas D_{3h} symmetry only requires 4 parameters. The figure of merit used to determine which symmetry best fits the data is reduced chi-squared, $\chi_v^2 = \frac{1}{DoF}\sum_i\left(1 - y_{calc,i}/y_{obs,i}\right)^2$, where y is the magnetic susceptibility or the energy of an excited state, and DoF (degrees of freedom) is the number of independent data (the number of 5f excited state transition energies observed plus the number of independent data in the magnetic susceptibility measurement) minus the number of parameters. The number of independent data in the magnetic susceptibility measurement may be estimated using van Vleck's second-order susceptibility formula, $\chi = \frac{N}{\sum p_i}\sum_i p_i\left(\frac{\left(E_i^{(1)}\right)^2}{kT} - 2E_i^{(2)}\right)$, where $p_i = exp\left(-E_i^{(0)}/kT\right)$, $E_i^{(1)} = \langle\psi_i|\mu_M|\psi_i\rangle$, and $E_i^{(2)} = \sum_j \frac{\left|\langle\psi_i|\mu_M|\psi_j\rangle\right|^2}{E_i^{(0)}-E_j^{(0)}}$.[57] The ground state provides two independent data, $E_0^{(1)}$ and $E_0^{(2)}$ ($E_0^{(0)}$ is zero and provides no information), and each excited state that becomes populated over the temperature range studied provides three independent data, $E_i^{(0)}$, $E_i^{(1)}$, and $E_i^{(2)}$. The population of an excited Kramer's doublet state is ca. 5 % when the thermal energy is 1/3 of $E_i^{(0)}$. Since *k*T at 300 K is 200 cm^{-1}, excited states with $E_i^{(0)} < 600$ cm^{-1} contribute the susceptibility at temperatures below 300 K.

Initial attempts to model the electronic structures of **1-3** using CONDON 3.0 included five observable transitions in the NIR for **1-3**. For **1**, the peaks at 7658 cm^{-1} and 7202 cm^{-1} were assumed to belong to single transition, and for **2**, the peaks at 7467 cm^{-1} and 7258 cm^{-1} were assumed to belong to single transition. While it was possible to identify parameters that reproduced five transitions with energies >5000 cm^{-1} using these assumptions, it was not possible to find parameters that reproduced both the transition energies and the magnetic data (magnetic susceptibilities and EPR g-values). Most notably, complex **2** has a low-lying excited state that could not be reproduced. In addition, studies of structurally-related bridging nitride and terminal nitride complexes indicate that these complexes have only four transitions with energies greater than 5000 cm^{-1}.[37, 38]

Based on the previous studies and the inability to identify suitable crystal field parameters to fit both the NIR and magnetic data, we hypothesize that only four transitions have energies greater than 5000 cm^{-1}, which is not consistent with the number of peaks observed. The most obvious explanation for the extra peaks is the presence of other compounds; however, the spectra of **1-3** were measured twice on independently-synthesized materials and the spectra did not vary between samples. Another possible explanation is vibronic coupling, which has previously been observed for $Np^{V}O_2^{2+}$ and $[U^{V}X_6]^-$ (X = Cl, Br).[30, 36, 47, 48, 58, 59] This explanation is plausible if the peaks displaying vibronic structure are associated with the U=E bond. Based upon the zeroth-order splitting of the $5f^1$ states, the peaks displaying vibronic structure likely involve $|1+\rangle$ and $|1-\rangle$, which are U=E π antibonding states. The peak corresponding to a final U=E σ antibonding state, $|0+\rangle$, does not display resolved vibronic structure, which is likely due to the fact that it is a shoulder on a much larger peak, and so the vibronic coupling is not observed. Moreover, the $|0+\rangle$ peak is broad, which is consistent with unresolved vibronic structure. As previously done for $[U^{V}X_6]^-$, the energies of the vibronic components of the transitions were averaged to determine the energy of the transitions.[58]

As noted above, the highest energy peak is due to a transition to $|0+\rangle$, and the other transitions may be tentatively assigned using the zeroth-order splitting shown in Figure 2. For **1**, the peaks at 7568 and 7202 cm^{-1} were averaged and are assumed to be arise from

$|1-\rangle$, whereas the peaks at 9973 and 9144 cm^{-1} were averaged and assigned to $|1+\rangle$. For **2**, the peaks at 9414 and 8734 cm^{-1} were averaged and assigned to $|1+\rangle$, whereas the peaks at 7467 and 7258 cm^{-1} were averaged and assigned to $|1-\rangle$. For **3**, the peaks at 9832 cm^{-1} and 8916 cm^{-1} were averaged and assigned to $|1+\rangle$. The peak at 7981 cm^{-1} was assigned to $|1-\rangle$ and does not appear to have vibronic structure. Finally, the lowest energy peak visible in the NIR was assigned to $|3+\rangle$. The transition energies are given in Table 2.

Table 2. Energies of the NIR states for complexes **1**-**3** and $[\mathrm{U^V(Tren^{TIPS})(N)}]^-$

Zeroth-order	[U]=NAd (**1**)		[U]=NR (**2**)		[U]=O (**3**)		$[\mathrm{U}]{\equiv}\mathrm{N}^{-\,a}$
assignment	Obs.^{b}	Avg.^{c}	Obs.^{b}	Avg.^{c}	Obs.^{b}	Avg.^{c}	Obs.^{b,c}
$|0+\rangle$	15434	15435	16955	16955	20262	20262^b	18000
$|1+\rangle$	9973 9144	9559	9414 8734	9077	9832 8916	9374	8900
$|1-\rangle$	7568 7202	7385	7467 7258	7363	7981	7981	6900
$|3+\rangle$	6245	6245	6097	6097	6022	6022	6060
$|2+\rangle$		--	--			--	4700

a) $[\mathrm{U^V(Tren^{TIPS})(N)}]^-$[37, 46]

b) Energy of observed peaks in the NIR spectrum

c) Vis-NIR transitions averaged to account for vibronic coupling (See text for discussion).

The transition energies and magnetic susceptibility data were first fit in D_{3h} symmetry using CONDON 3.0 with initial parameters determined by fitting the energies of the NIR peaks using the zeroth-order model shown in Figure 2. For **1** and **3**, the D_{3h} model included an additional state just above 5000 cm^{-1}, which is not consistent with the observed NIR spectrum (the results of this analysis are summarized in Table 3).

However, lowering the symmetry to C_{3v} produces fits with only four states with energies greater than 5000 cm^{-1}, in agreement with the observed NIR spectra (fitting parameters are given in Table 4 and energies of the states are given in Table 5). In addition, the fitting in C_{3v} symmetry produced better agreement than in D_{3h} symmetry as judged by the value of χ_v^2 (Table 4), which is based on the fit of the model to the NIR transition energies and the variable temperature magnetic susceptibility. The fit in C_{3v} symmetry also produces good agreement between the measured and modeled magnetic susceptibilities as shown in Figure 6, and the energies of the f-f transitions are also in good agreement with observation, which may be seen by comparing Tables 2 and 5. In addition, C_{3v} is closer to the actual symmetry of the molecules than is D_{3h}.

In contrast to the energies of the states, the main component of the states in Table 5 are not in complete agreement with the zeroth-order prediction in Figure 2. In **3**, the only difference is a reversal of the order of the lowest two states due its trigonal pyramidal geometry, as discussed above. For **1** and **2**, the differences are related to mixing of states allowed in C_{3v} symmetry. In particular, in **1**, the $|1-\rangle$ and $|2+\rangle$ states can mix because the Kramers doublet pair of $|1-\rangle$ is $|-1+\rangle$ ($m_j = -1/2$), which has a value of m_j that is 3 less than that of $|2+\rangle$ ($m_j = 5/2$). As a result of this mixing, the $|1+\rangle$ state in the zeroth-order model has more $|2+\rangle$ character than $|1+\rangle$ character (Table S4). In addition, the ordering of the states of **1** determined by crystal field modeling are in agreement with the states of $[U^{V}(Tren^{TIPS})(N)]^{-}$ as determined by *ab initio* calculation,[37] which is reassuring since both complexes possess similar pseudotetrahedral geometries. In **2**, the $|1-\rangle$ ($m_j = 1/2$) and $|3+\rangle$ ($m_j = 7/2$) states are strongly mixed by the crystal field, changing the ordering of the states predicted by the simple zeroth-order model and determined by crystal field fitting.

As a result, both states labeled $|1-\rangle$ in Table 5 are mixtures of the $|1-\rangle$ and $|3+\rangle$ states, with the lower energy $|1-\rangle$ state containing slightly more $|1-\rangle$ character than $|3+\rangle$ character. Overall, the zeroth-order prediction of the ordering of the states in these complexes is in agreement with the ordering observed in the crystal field model once the effects of lowering the symmetry from D_{3h} to C_{3v} are taken into account.

Table 3. Calculated energies and the contribution of the largest $|m_l\ m_s\rangle$ components of the 5f states for complexes **1-3** in D_{3h} symmetry[a].

[U]=NAd (**1**)	[U]=NSiMe$_3$ (**2**)	[U]=O (**3**)
0.95 $|0+\rangle$, 15437 cm^{-1}	0.98 $|0-\rangle$, 17009 cm^{-1}	0.98 $|0+\rangle$, 20262 cm^{-1}
0.92 $|1+\rangle$, 9568 cm^{-1}	0.98 $|1+\rangle$, 9257 cm^{-1}	0.95 $|1+\rangle$, 9302 cm^{-1}
0.97 $|2+\rangle$, 7379 cm^{-1}	0.98 $|1-\rangle$, 7364 cm^{-1}	0.92 $|3+\rangle$, 7975 cm^{-1}
0.93 $|1-\rangle$, 6240 cm^{-1}	0.88 $|3+\rangle$, 6056 cm^{-1}	0.98 $|1-\rangle$, 6081 cm^{-1}
1.00$|3+\rangle$, 5039 cm^{-1}	0.88 $|2+\rangle$, 3283 cm^{-1}	0.85 $|2+\rangle$, 5267 cm^{-1}
0.92 $|2-\rangle$, 2859 cm^{-1}	0.84 $|3-\rangle$, 19 cm^{-1}	0.85 $|3-\rangle$, 603 cm^{-1}
0.97 $|3-\rangle$	0.98 $|2-\rangle$	0.95 $|2-\rangle$

a) m_s is represented by "+" for +1/2 and "-" for -1/2.

Table 4. Summary of crystal field fitting for **1-3** in C_{3v} symmetry using CONDON 3.0

	[U]=NAd (**1**)	[U]=NSiMe$_3$ (**2**)	[U]=O (**3**)
B_2^0 (cm^{-1})	11469	12402	14177
B_4^0 (cm^{-1})	13312	22744	26420
B_6^0 (cm^{-1})	9744	8272	14747
B_6^6 (cm^{-1})	1971	7634	6491
B_4^3 (cm^{-1})	-6498	-7115	-6340
B_6^3 (cm^{-1})	-3161	3307	10484
ζ (cm^{-1})	1730	1298	1351
$g_{\|}$ (exp)	3.60	2.50	2.17
$g_{\|}$ (calc)	4.05	2.79	1.91
# of parameters	7	7	7
# of independent data	6	9	9
χ_v^2 [a]	(0.52)[b]	0.27	0.12
χ_v^2 [a] (D_{3h})	1.51	0.95	0.49

a) $\chi_v^2 = \frac{1}{DoF}\sum_i\left(1 - y_{calc,i}/y_{obs,i}\right)^2$, DoF = # of independent data - # of parameters

b) Three times the value with 1 degree of freedom (allows comparison to χ_v^2 in D_{3h} symmetry)

Table 5. Calculated energies and the contribution of the largest $|m_l\, m_s\rangle$ components of the 5f states for complexes **1-3** in C_{3v} symmetry [a]

[U]=NAd (**1**)	[U]=NSiMe$_3$ (**2**)	[U]=O (**3**)
0.93 $|0+\rangle$, 15433 cm^{-1}	0.94 $|0-\rangle$, 16955 cm^{-1}	0.93 $|0+\rangle$, 20262 cm^{-1}
0.81 $|1+\rangle$, 9559 cm^{-1}	0.97 $|1+\rangle$, 9054 cm^{-1}	0.75 $|1+\rangle$, 9373 cm^{-1}
0.80 $|2+\rangle$, 7385 cm^{-1}	0.73 $|1-\rangle$, 7364 cm^{-1}	0.78 $|1-\rangle$, 7981 cm^{-1}
0.93 $|3+\rangle$, 6245 cm^{-1}	0.65 $|1-\rangle$, 6097 cm^{-1}	0.81 $|3+\rangle$, 6022 cm^{-1}
0.76 $|1-\rangle$, 4680 cm^{-1}	0.89 $|2+\rangle$, 3758 cm^{-1}	0.78 $|2+\rangle$, 3522 cm^{-1}
0.92 $|2-\rangle$, 1119 cm^{-1}	0.97 $|2-\rangle$, 156 cm^{-1}	0.83 $|3-\rangle$, 313 cm^{-1}
0.92 $|3-\rangle$	0.84 $|3-\rangle$	0.94 $|2-\rangle$

a) m_s is represented by "+" for +1/2 and "-" for -1/2.

Rather than discuss the relationship between the parameters given in Tables 4 and 5 and the structures of the complexes, it seems more instructive to determine the energies of the 5f orbitals in the absence of SOC and compare how the geometries of the complexes affect the orbital energies. Accordingly, the orbital energies are given in Table 6, and the experimentally derived MO diagrams for complexes **1-3** are shown in Figure 7. Most importantly, we observed that changes in electronic structure are primarily related to the steric bulk of the E^{2-} ligand, which affects both the metal-ligand bond lengths and inter-ligand angles of the complexes.

Table 6. 5f orbital energies in cm^{-1} determined from the parameters in Table 4[a]

	[U]=NAd (**1**)	[U]=NSiMe$_3$ (**2**)	[U]=O (**3**)
f_σ	11473	15116	18100
f_π	4988	6591	6533
f_φ	1099	4531	3774
f_δ	713	621	0
f_φ	0	0	229

a) m$_s$ is represented by "+" for +1/2 and "-" for -1/2.

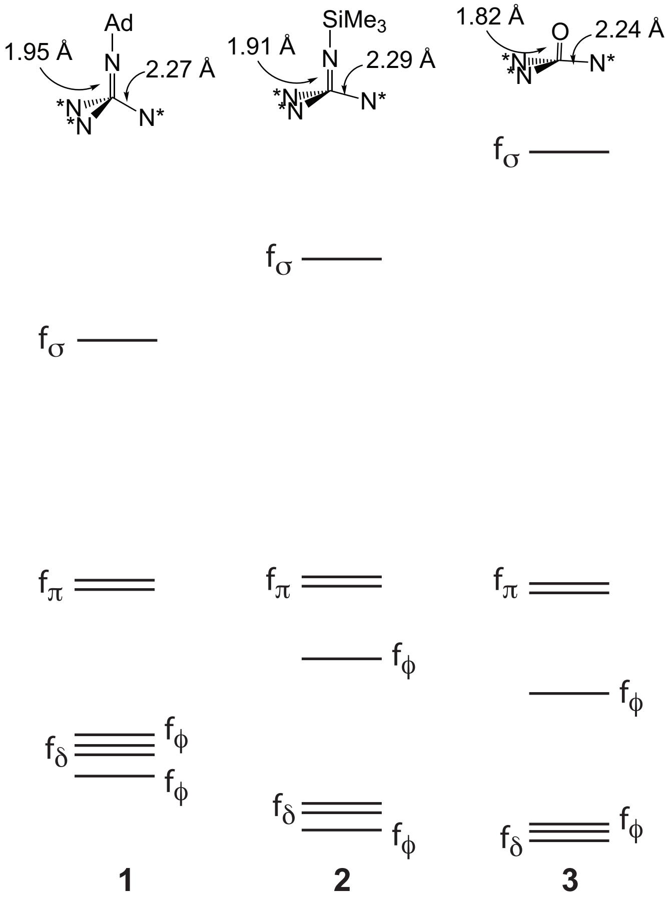

Figure 7. Experimentally derived MO diagrams for **1-3**, drawn with a fixed average 5f orbital energy (barycenter). N* = N(SiMe$_3$)$_2$.

Changing the steric bulk of the E^{2-} ligand has two effects on the geometries of **1-3**: (1) decreasing steric bulk leads to shorter metal-ligand bond lengths, especially for the

U=E bond, and (2) decreasing steric bulk changes the geometry of the complexes from pseudotetrahedral (in **1**) to trigonal pyramidal geometry (in **3**), with **2** having an intermediate geometry. The obvious effect of decreasing bond lengths is to increase the splitting of the f orbitals shown in Figure 7. This is especially noticeable in the energies of the |0+⟩ σ* states; the relationship between bond length and transition energies for the other states is weaker (Figure S4). Changing the steric bulk of the E^{2-} ligand also alters the geometry of the complex, which primarily affects the low-lying f_φ and f_δ orbitals. For example, the U atom in **3** lies very close to the plane defined by the three N atoms of the NR_2 ligands. In addition, the O-U-N-Si torsion angle is 30°, which places the π-donating N 2p orbital largely in the plane defined by U atom and the three N atoms of the NR_2 ligands. As a result of these factors, one of the f_φ orbitals is σ antibonding with respect to the three NR_2 ligands and the other f_φ orbital is π antibonding with respect to the NR_2 ligands, which raises their energies. The f_δ orbitals have little if any overlap with either the E or NR_2 orbitals and are non-bonding or very nearly non-bonding. For this reason, the f_δ orbitals are lowest in energy, and the ground state is |2-⟩. In contrast, in **1**, the steric bulk of the adamantyl substituent produces a pseudotetrahedral geometry, wherein the U atom no longer lies in the plane defined by three N atoms of the NR_2 ligands. As a result, the f_δ orbitals and one of the f_φ orbitals in **1** become σ antibonding with respect to the NR_2 ligands. Due to this change, the f_δ orbitals of **1** are destabilized and the f_δ and f_φ orbitals become similar in energy. None of the low-lying orbitals of **1** are non-bonding; they are all weakly σ and π antibonding with respect to the three NR_2 ligands. These interactions have two effects on the electronic structure of **1** relative to **3**. First, the ground state in **1** is |3-⟩ due to the destabilization of the f_δ relative to **3**. Second, the NIR transitions are lower in energy than they would be if the ground state were non-bonding. The electronic structure of **2** more closely resembles that of **3** than that of **1**, with one important difference: the bulk of the imido $SiMe_3$ substituent creates a larger N_{imido}-U-NR_2 angle than the O-U-NR_2 angle in **3**. As a result, the f_δ orbitals become slightly destabilized such that the ground state of **2** is $|3\text{-}\rangle$ rather than $|2\text{-}\rangle$ in **3**.

Interestingly, the energy of $|0+\rangle$ state in **3** is ~2000 cm^{-1} greater than the analogous energy in $[(Tren^{TIPS})U^{V}(N)]^{-}$, despite the fact that the U=E distances in these complexes are nearly identical.[37] Part of the reason for this difference is that $[(Tren^{TIPS})U^{V}(N)]^{-}$ has a pseudotetrahedral geometry similar to that of **1**, so the ground state of $[(Tren^{TIPS})U^{V}(N)]^{-}$ will be slightly antibonding and destabilized relative to the ground state of **3**. The other difference is the orbital energies of O^{2-} vs N^{3-}. Because O^{2-} has a lower charge than N^{3-}, and because O is more electronegative than N, the 2s and 2p orbitals of an isolated O^{2-} fragment are expected to be lower in energy than those of an isolated N^{3-} fragment. As shown by Burdett, the destabilization of the metal-based anti-bonding orbitals is directly proportional to the stability of the ligand orbitals.[60] In other words, there are two main factors that affect the energies of the 5f-based antibonding orbitals: (1) the strength of the interaction between the metal and ligand orbitals and (2) the energies of the ligand orbitals. Because we cannot deconvolute these factors, we cannot conclude that the greater U=E σ^* energy of **3** relative to that of $[(Tren^{TIPS})U^{V}(N)]^{-}$ implies that the U=O interaction is stronger than the U≡N interaction. The same phenomena may also contribute to the observation that the 5f σ^* state of **1** is ~1500 cm^{-1} higher in energy than in **2**.[61] The trimethylsilyl group in **2** is less strongly electron donating than the 1-adamantyl group in **1**, as indicated by their Hammett σ_p parameters, which are -0.07 and -0.13, respectively.[62] As a result, the silylimido ligand orbitals will be slightly more stable than the alkylimido ligand orbitals, so the 5f σ* state of **2** will be lower in energy than that of **1**, even if orbital mixing were identical in the two complexes. The U=N distance of **1** is also longer than the U=N distance of **2**, which further contributes to the difference between the energies of the 5f σ* states. As seen in the oxo/nitrido comparison, the relative contributions of bond distance and stability of the imido fragment to the energies of the 5f σ* cannot be deconvoluted using the available data. Destabilization of the 5f σ* states due to the stabilization of the ligand orbitals is also observed in $[U^{V}X_6]^-$ and $[U^{IV}X_6]^{2-}$, which strongly affects the energies of the 5f states.[31, 63] Perhaps more importantly, because of electrostatic effects, the degree of orbital mixing and stabilization for U=E bonding orbitals does not necessarily correlate with bond strength. A similar conclusion was drawn by Maron and Eisenstein in a computational study of tetravalent uranium oxo and imido complexes.[64]

Limitations of crystal field modeling. Three main issues affect the accuracy of electronic structure models produced using crystal field theory. The first issue is the reliance on accurate measurements. For magnetic susceptibility measurements, the samples must be sufficiently pure, and the magnetism of the sample holder must be accurately subtracted, for these data to be useful. Generally speaking, these requirements are straightforward to achieve, which is why CONDON 3.0 is an attractive code for investigating the electronic structures of actinides. The second issue is the interpretation of the visible and NIR spectra, especially with respect to possible vibronic structure. In addition, the transition energy modeled in crystal field fitting is the zero phonon energy (transitions between the lowest vibrational states of the ground and excited states), which may not be the center of the peak, as we have assumed here. For narrow f-f transitions, the error is likely small; however, for broad transitions, such as that to the $|0+\rangle$ state, the error can be larger. Relatedly, the $|0+\rangle$ peaks are all shoulders on stronger transitions at higher energy, which decreases the accuracy of the energy assigned to these transitions. The third issue is the manner in which orbital mixing affects the crystal field model. Its main impact for f^1 systems is to reduce SOC by decreasing orbital angular momentum. In the crystal field model used here, reduction of angular momentum is the same for all orbitals and is implemented by allowing the SOC constant to vary. However, orbital mixing and the associated reduction in SOC are actually different for the different orbitals. Mixing is largest for f_σ, smaller for f_π, and much smaller for the other f orbitals. These differences in orbital mixing can affect the magnetic properties of the complexes but cannot be modeled without introducing additional parameters.

Finally, in this study, the data-to-parameter ratio is low, especially for **1**, which tends to increase the uncertainty in the resulting fitted parameters. For **1**, in particular, there are insufficient data to accommodate the seven parameters needed to perform a fit in C_{3v} symmetry. As a result, the uncertainties on the fitted parameters will be large. Likewise, the uncertainties on the energies of the orbitals and the mixing of the orbitals will be large, as discussed above. Finally, the data may not uniquely define a set of parameters for **1**. In spite of these limitations, the modeling the electronic structures of **1-3** using crystal field theory provides a clear picture of the role of ligands in determining the electronic structure.

Conclusions

We have prepared a series of multiply-bonded U(V) complexes and investigated their electronic structures using a combination of magnetic susceptibility, EPR spectroscopy, NIR spectroscopy, and crystal field modeling. We find that, within this series of complexes, the steric bulk of the E^{2-} (E = O, NR) ligand is the most important factor in determining the electronic structure, since it changes both the metal-ligand bond lengths and inter-ligand angles of the complex. Most dramatically, these structural changes result in a switch in the lowest energy f orbital, from f_{ϕ} for the imido complexes to f_{δ} in the oxo complex. Surprisingly, the 5f orbital splitting in the U(V) oxo complex is greater than the analogous splitting for a pentavalent uranium nitride complex. However, this difference is likely due to greater stability of the bonding orbitals in the oxo ligand vs. those of nitrido ligand combined with the destabilization of the f_{δ} orbitals in the nitride complex due to its pseudotetrahedral geometry, rather than due to a stronger interaction between the oxo ligand and the 5f orbitals. Because the overall strengths of U=E bonds do not correlate well with the degree of covalency, estimating the strengths of these bonds from the splitting of the 5f states is not possible. On the other hand, because the ligands affect the 5f orbitals and states in predictable manner, the insights gained herein may be useful for those wanting to control the electronic structures of related actinide complexes, especially if the goal is to study (and tailor) magnetic properties. This control is especially relevant for U(V) complexes, as they are known to exhibit single molecule magnet (SMM) behavior.[53, 65]

Experimental

General. All reactions and subsequent manipulations were performed under anaerobic and anhydrous conditions under an atmosphere of nitrogen. Hexanes and diethyl ether (Et_2O) were dried using a Vacuum Atmospheres DRI-SOLV Solvent Purification system and stored over 3Å sieves for 24 h prior to use. All deuterated solvents were purchased from Cambridge Isotope Laboratories Inc. and were dried over activated 3 Å molecular sieves for 24 h prior to use. $[U^{III}(NR_2)_3]$ ($R = SiMe_3$),[66] $[U^{V}(NR_2)_3(O)]$,[40] $[U^{V}(NR_2)_3(NSiMe_3)]$,[39] were synthesized according to published procedures. All other reagents were obtained from commercial sources and used as received.

NMR spectra were recorded on a Varian UNITY INOVA AS600 spectrometer. ^1H NMR spectra were referenced to external $SiMe_4$ using the residual protio solvent peaks as internal standards. IR spectra were recorded on a Nicolet 6700 FT-IR spectrometer. UV-Vis-NIR experiments were performed on a UV-3600 Shimadzu spectrophotometer and fit to pseudoVoigt peaks using Excel.

Electron paramagnetic resonance (EPR) spectra were obtained at 3 K with a Varian E-12 spectrometer equipped with a liquid helium cryostat, an EIP-547 microwave frequency counter, and a Varian E-500 gaussmeter, which was calibrated using 2,2-diphenyl-1-picrylhydrazyl (DPPH, $g = 2.0036$).

Magnetic properties were recorded using a Quantum Design Magnetic Property Measurement System SQUID vibrating sample magnetometer (MPMS3 SQUID-VSM), located within the MRL Shared Experimental Facilities. 15-25 mg samples of polycrystalline material were loaded into a glass NMR tube, which was subsequently flame sealed under static vacuum. The solids were kept in place by quartz wool packed on either side of the sample. DC magnetic measurements were performed in VSM mode while sweeping either the applied magnetic field or temperature at controlled rates. For the magnetic susceptibility measurements, diamagnetic corrections (χ_{dia} = -493×10^{-6} cm^3/mol for **1**, χ_{dia} = -446×10^{-6} cm^3/mol for **2**) were made using Pascal's constants.[67] The data were corrected for the contribution from the quartz wool or sample holder by subtracting the magnetization of an NMR tube containing quartz wool.

Synthesis of [U^V(NR$_2$)$_3$(NAd)] (1). To a stirring solution of [U^{III}(NR$_2$)$_3$] (0.135 g, 0.187 mmol) in Et$_2$O (5 mL) was added a solution of 1-azidoadamantane (0.0332 g, 0.187 mmol) in Et$_2$O (1.5 mL). The addition resulted in a rapid color change from deep purple to deep green, concomitant with the evolution of gas. After stirring for 15 min, the solution volume was reduced *in vacuo* to 5 mL. Subsequent storage of this solution at -25 °C overnight resulted in the deposition of dark green needles (0.090 g, 56%). Anal. Calcd for $C_{28}H_{69}N_4Si_6U$: C, 38.73; H, 8.01; N, 6.45. Found: C, 38.74; H, 8.03; N, 6.34. ^{1}H NMR (600 MHz, 25 °C, C_6D_6): δ -3.92 (br s, 54H, CH$_3$), 8.44 (s, 3H, CH$_2$), 10.53 (s, 3H, CH$_2$), 16.72 (s, 3H, CH), 20.02 (br s, 6H, CH$_2$). IR (KBr pellet, cm^{-1}): 607 (s), 660 (s), 771 (s), 843 (vs), 899 (vs), 1095(m), 1122 (m), 1178 (m), 1254 (s), 1300 (m), 1342 (w), 1363 (w), 1402 (m), 1450 (m), 2852 (m), 2908 (s), 2951 (s).

X-Ray Crystallography. Data for **1** were collected on a Bruker KAPPA APEX II diffractometer equipped with an APEX II CCD detector using a TRIUMPH monochromator with a Mo Kα X-ray source (α = 0.71073 Å). The crystals were mounted on a cryoloop under Paratone-N oil, and all data were collected at 100(2) K using an Oxford nitrogen gas cryostream. Data were collected using ω scans with 0.5° frame widths and frame exposures of 10 s. Data collection and cell parameter determination were conducted using the SMART program.[68] Integration of the data frames and final cell parameter refinement were performed using SAINT software.[69] Absorption correction of the data was carried out using the multi-scan method SADABS.[70] Subsequent calculations were carried out using SHELXTL.[71] Structure determination was done using direct or Patterson methods and difference Fourier techniques. All hydrogen atom positions were idealized, and rode on the atom of attachment. Structure solution, refinement, graphics, and creation of publication materials were performed using SHELXTL.[71] Further crystallographic details can be found in Table S1. Complex **1** has been deposited in the Cambridge Structural Database (CCDC 2239158).

Crystal Field Fitting. Variable temperature molar magnetic susceptibility between 10 K and 300 K and the energies of the 5f-5f transitions were modeled using the program CONDON 3.0. Magnetic susceptibility measured at temperatures below 10 K were not included because intermolecular interactions, especially dipole-dipole coupling, can decrease the magnetic susceptibility. Since the magnetic susceptibility measurement includes ~100 data points, but only 2 or 5 independent data, each of the 100 data points was given 1/10 of the weight of the excited state energies in the fit. Fitting was initially performed in D_{3h} symmetry. Starting values of the crystal field parameters and spin orbit coupling were varied until the fit could not be improved. Once the best fit values were identified, the fit was repeated in C_{3v} symmetry by giving B_4^3 and B_6^3 starting values of ±4000 cm^{-1} (the starting values for the other parameters were those from the fit in D_{3h} symmetry). The orbital energies were determined by assigning ζ to a small value and using the B_x^y parameters determined from the fits.

ASSOCIATED CONTENT

Supporting Information. Experimental procedures, crystallographic details, and spectral data for complexes **1**-**3** (PDF).

AUTHOR INFORMATION

Corresponding Author

hayton@chem.ucsb.edu, wwlukens@lbl.gov

Conflict of Interest

The authors declare no competing financial interests.

ACKNOWLEDGMENTS

This work was supported by the U.S. Department of Energy, Office of Basic Energy Sciences, Chemical Sciences, Biosciences, and Geosciences Division, under Contract DE-SC0001861. The MRL Shared Experimental Facilities are supported by the MRSEC Program of the NSF under Award No. DMR 1720256; a member of the NSF-funded Materials Research Facilities Network (www.mrfn.org). The electronic structure analysis was supported by U.S. Department of Energy, Basic Energy Sciences, Chemical Sciences, Biosciences, and Geosciences Division, Heavy Element Chemistry Program and was performed at Lawrence Berkeley National Laboratory under Contract No. DE-AC02-05CH11231. WWL gratefully thanks Jan van Leusen for detailed instructions on using CONDON 3.0. THN and TWH thank Guang Wu for help with the X-ray crystallographic analysis.

References

1. Kozimor, S. A.; Yang, P.; Batista, E. R.; Boland, K. S.; Burns, C. J.; Clark, D. L.; Conradson, S. D.; Martin, R. L.; Wilkerson, M. P.; Wolfsberg, L. E., Trends in Covalency for d- and f-Element Metallocene Dichlorides Identified Using Chlorine K-Edge X-ray Absorption Spectroscopy and Time-Dependent Density Functional Theory. *J. Am. Chem. Soc.* **2009**, *131*, 12125-12136.
2. Minasian, S. G.; Keith, J. M.; Batista, E. R.; Boland, K. S.; Clark, D. L.; Conradson, S. D.; Kozimor, S. A.; Martin, R. L.; Schwarz, D. E.; Shuh, D. K.; Wagner, G. L.; Wilkerson, M. P.; Wolfsberg, L. E.; Yang, P., Determining Relative f and d Orbital Contributions to M–Cl Covalency in MCl_6^{2-} (M = Ti, Zr, Hf, U) and $UOCl_5^{-}$ Using Cl K-Edge X-ray Absorption Spectroscopy and Time-Dependent Density Functional Theory. *J. Am. Chem. Soc.* **2012**, *134*, 5586-5597.
3. Minasian, S. G.; Keith, J. M.; Batista, E. R.; Boland, K. S.; Clark, D. L.; Kozimor, S. A.; Martin, R. L.; Shuh, D. K.; Tyliszczak, T., New evidence for 5f covalency in actinocenes determined from carbon K-edge XAS and electronic structure theory. *Chem. Sci.* **2014**, *5*, 351-359.
4. Cross, J. N.; Su, J.; Batista, E. R.; Cary, S. K.; Evans, W. J.; Kozimor, S. A.; Mocko, V.; Scott, B. L.; Stein, B. W.; Windorff, C. J.; Yang, P., Covalency in Americium(III) Hexachloride. *J. Am. Chem. Soc.* **2017**, *139*, 8667-8677.
5. Su, J.; Batista, E. R.; Boland, K. S.; Bone, S. E.; Bradley, J. A.; Cary, S. K.; Clark, D. L.; Conradson, S. D.; Ditter, A. S.; Kaltsoyannis, N.; Keith, J. M.; Kerridge, A.; Kozimor, S. A.; Löble, M. W.; Martin, R. L.; Minasian, S. G.; Mocko, V.; La Pierre, H. S.; Seidler, G. T.; Shuh, D. K.; Wilkerson, M. P.; Wolfsberg, L. E.; Yang, P., Energy-Degeneracy-Driven Covalency in Actinide Bonding. *J. Am. Chem. Soc.* **2018**, *140*, 17977-17984.
6. Qiao, Y.; Ganguly, G.; Booth, C. H.; Branson, J. A.; Ditter, A. S.; Lussier, D. J.; Moreau, L. M.; Russo, D. R.; Sergentu, D.-C.; Shuh, D. K.; Sun, T.; Autschbach, J.; Minasian, S. G., Enhanced 5f-δ bonding in $[U(C_7H_7)_2]^{-}$: C K-edge XAS, magnetism, and *ab initio* calculations. *Chem. Commun.* **2021**, *57*, 9562-9565.
7. Zhang, Y.; Duan, W.; Yang, Y.; Jian, T.; Qiao, Y.; Ren, G.; Zhang, N.; Zheng, L.; Yan, W.; Wang, J.; Chen, J.; Minasian, S. G.; Sun, T., Involvement of 5f Orbitals in the Covalent Bonding between the Uranyl Ion and Trialkyl Phosphine Oxide: Unraveled by Oxygen K-Edge X-ray Absorption Spectroscopy and Density Functional Theory. *Inorg. Chem.* **2022**, *61*, 92-104.
8. Sergentu, D.-C.; Autschbach, J., Covalency in actinide(iv) hexachlorides in relation to the chlorine K-edge X-ray absorption structure. *Chem. Sci.* **2022**, *13*, 3194-3207.
9. Gaunt, A. J.; Reilly, S. D.; Enriquez, A. E.; Scott, B. L.; Ibers, J. A.; Sekar, P.; Ingram, K. I. M.; Kaltsoyannis, N.; Neu, M. P., Experimental and Theoretical Comparison of Actinide and Lanthanide Bonding in $M[N(EPR_2)_2]_3$ Complexes (M = U, Pu, La, Ce; E = S, Se, Te; R = Ph, ^{i}Pr, H). *Inorg. Chem.* **2008**, *47*, 29-41.

10. Gianopoulos, C. G.; Zhurov, V. V.; Minasian, S. G.; Batista, E. R.; Jelsch, C.; Pinkerton, A. A., Bonding in Uranium(V) Hexafluoride Based on the Experimental Electron Density Distribution Measured at 20 K. *Inorg. Chem.* **2017**, *56*, 1775-1778.
11. Zhurov, V. V.; Zhurova, E. A.; Pinkerton, A. A., Chemical Bonding in Cesium Uranyl Chloride Based on the Experimental Electron Density Distribution. *Inorg. Chem.* **2011**, *50*, 6330-6333.
12. Zhurov, V. V.; Zhurova, E. A.; Stash, A. I.; Pinkerton, A. A., Characterization of Bonding in Cesium Uranyl Chloride: Topological Analysis of the Experimental Charge Density. *J. Phys. Chem. A* **2011**, *115*, 13016-13023.
13. Smiles, D. E.; Wu, G.; Hrobárik, P.; Hayton, T. W., Use of ^{77}Se and ^{125}Te NMR Spectroscopy to Probe Covalency of the Actinide-Chalcogen Bonding in $[Th(E_n)\{N(SiMe_3)_2\}_3]^-$ (E = Se, Te; $n = 1, 2$) and Their Oxo-Uranium(VI) Congeners. *J. Am. Chem. Soc.* **2016**, *138*, 814-825.
14. Kent, G.; Yu, X.; Wu, G.; Autschbach, J.; Hayton, T. W., Ring-opening of a Thorium Cyclopropenyl Complex Generates a Transient Thorium-bound Carbene. *Chem. Commun.* **2022**, *58*, 6805-6808.
15. Kent, G. T.; Yu, X.; Wu, G.; Autschbach, J.; Hayton, T. W., Synthesis and electronic structure analysis of the actinide allenylidenes, $[\{(NR_2)_3\}An(CCCPh_2)]^-$ (An = U, Th; R = $SiMe_3$). *Chem. Sci.* **2021**, *12*, 14383-14388.
16. Ordoñez, O.; Yu, X.; Wu, G.; Autschbach, J.; Hayton, T. W., Synthesis and Characterization of Two Uranyl-Aryl "Ate" Complexes. *Chem. Eur. J.* **2021**, *27*, 5885-5889.
17. Ordoñez, O.; Yu, X.; Wu, G.; Autschbach, J.; Hayton, T. W., Homoleptic Perchlorophenyl "Ate" Complexes of Thorium(IV) and Uranium(IV). *Inorg. Chem.* **2021**, *60*, 12436-12444.
18. Sergentu, D.-C.; Kent, G. T.; Staun, S. L.; Yu, X.; Cho, H.; Autschbach, J.; Hayton, T. W., Probing the Electronic Structure of a Thorium Nitride Complex by Solid-State ^{15}N NMR Spectroscopy. *Inorg. Chem.* **2020**, *59*, 10138-10145.
19. Seaman, L. A.; Hrobárik, P.; Schettini, M. F.; Fortier, S.; Kaupp, M.; Hayton, T. W., A Rare Uranyl(VI)–Alkyl Ate Complex $[Li(DME)_{1.5}]_2[UO_2(CH_2SiMe_3)_4]$ and Its Comparison with a Homoleptic Uranium(VI)–Hexaalkyl. *Angew. Chem. Int. Ed.* **2013**, *52*, 3259-3263.
20. Smiles, D. E.; Wu, G.; Hrobárik, P.; Hayton, T. W., Synthesis, Thermochemistry, Bonding, and ^{13}C NMR Chemical Shift Analysis of a Phosphorano-Stabilized Carbene of Thorium. *Organometallics* **2017**, *36*, 4519-4524.
21. Réant, B. L. L.; Berryman, V. E. J.; Basford, A. R.; Nodaraki, L. E.; Wooles, A. J.; Tuna, F.; Kaltsoyannis, N.; Mills, D. P.; Liddle, S. T., ^{29}Si NMR Spectroscopy as a Probe of s- and f-Block Metal(II)–Silanide Bond Covalency. *J. Am. Chem. Soc.* **2021**, *143*, 9813-9824.
22. Mullane, K. C.; Hrobárik, P.; Cheisson, T.; Manor, B. C.; Carroll, P. J.; Schelter, E. J., ^{13}C NMR Shifts as an Indicator of U–C Bond Covalency in Uranium(VI) Acetylide Complexes: An Experimental and Computational Study. *Inorg. Chem.* **2019**, *58*, 4152-4163.
23. Du, J.; Seed, J. A.; Berryman, V. E. J.; Kaltsoyannis, N.; Adams, R. W.; Lee, D.; Liddle, S. T., Exceptional uranium(VI)-nitride triple bond covalency from ^{15}N nuclear

magnetic resonance spectroscopy and quantum chemical analysis. *Nature Commun.* **2021**, *12*, 5649.

24. Staun, S. L.; Sergentu, D.-C.; Wu, G.; Autschbach, J.; Hayton, T. W., Use of ^{15}N NMR spectroscopy to probe covalency in a thorium nitride. *Chem. Sci.* **2019**, *10*, 6431-6436.

25. Pedrick, E. A.; Hrobárik, P.; Seaman, L. A.; Wu, G.; Hayton, T. W., Synthesis, structure and bonding of hexaphenyl thorium(iv): observation of a non-octahedral structure. *Chem. Commun.* **2016**, *52*, 689-692.

26. Formanuik, A.; Ariciu, A.-M.; Ortu, F.; Beekmeyer, R.; Kerridge, A.; Tuna, F.; McInnes, E. J. L.; Mills, D. P., Actinide covalency measured by pulsed electron paramagnetic resonance spectroscopy. *Nature Chem.* **2017**, *9*, 578-583.

27. Rao, G.; Altman, A. B.; Brown, A. C.; Tao, L.; Stich, T. A.; Arnold, J.; Britt, R. D., Metal Bonding with 3d and 6d Orbitals: An EPR and ENDOR Spectroscopic Investigation of Ti^{3+}–Al and Th^{3+}–Al Heterobimetallic Complexes. *Inorg. Chem.* **2019**, *58*, 7978-7988.

28. Gourier, D.; Caurant, D.; Arliguie, T.; Ephritikhine, M., EPR and Angle-Selected ENDOR Study of 5f-Ligand Interactions in the $[U(\eta^7\text{-}C_7H_7)_2]^-$ Anion, an f^1 Analogue of Uranocene. *J. Am. Chem. Soc.* **1998**, *120*, 6084-6092.

29. Kolbe, W.; Edelstein, N., Electron-Nuclear Double Resonance of Pu^{3+} in CaF_2. *Phys. Rev. B* **1971**, *4*, 2869-2875.

30. Edelstein, N.; Brown, D.; Whittaker, B., Covalency Effects on the Ligand Field Splittings of Octahedral $5f^1$ Compounds. *Inorg. Chem.* **1974**, *13*, 563-567.

31. Lukens, W. W.; Edelstein, N. M.; Magnani, N.; Hayton, T. W.; Fortier, S.; Seaman, L. A., Quantifying the σ and π Interactions between U(V) f Orbitals and Halide, Alkyl, Alkoxide, Amide and Ketimide Ligands. *J. Am. Chem. Soc.* **2013**, *135*, 10742-10754.

32. Seaman, L. A.; Wu, G.; Edelstein, N.; Lukens, W. W.; Magnani, N.; Hayton, T. W., Probing the 5f Orbital Contribution to the Bonding in a U(V) Ketimide Complex. *J. Am. Chem. Soc.* **2012**, *134*, 4931-4940.

33. Notter, F.-P.; Bolvin, H., Optical and magnetic properties of the $5f^1$ AnX_6^{q-} series: A theoretical study. *J. Chem. Phys.* **2009**, *130*, 184310.

34. Krupa, J. C.; Hussonois, M.; Genet, M.; Guillaumont, R., Optical spectra of Pa^{4+} diluted in $ThCl_4$ single crystals. *J. Chem. Phys.* **1982**, *77*, 154-158.

35. Eisenstein, J. C.; Pryce, M. H. L., Electronic structure and magnetic properties of the neptunyl ion. *Journal of research of the National Bureau of Standards. Section A, Physics and chemistry* **1965**, *69a*, 217-235.

36. Denning, R. G.; Norris, J. O. W.; Brown, D., The electronic structure of actinyl ions. *Mol. Phys.* **1982**, *46*, 287-323.

37. King, D. M.; Cleaves, P. A.; Wooles, A. J.; Gardner, B. M.; Chilton, N. F.; Tuna, F.; Lewis, W.; McInnes, E. J. L.; Liddle, S. T., Molecular and electronic structure of terminal and alkali metal-capped uranium(V) nitride complexes. *Nature Commun.* **2016**, *7*, 13773.

38. Staun, S. L.; Wu, G.; Lukens, W. W.; Hayton, T. W., Synthesis of a heterobimetallic actinide nitride and an analysis of its bonding. *Chem. Sci.* **2021**, *12*, 15519-15527.

39. Zalkin, A.; Brennan, J. G.; Andersen, R. A., Tris[bis(trimethylsilyl)amido](trimethylsilylimido)uranium(V). *Acta Crystallogr., Sect. C* **1988**, *44*, 1553-1554.
40. Fortier, S.; Brown, J. L.; Kaltsoyannis, N.; Wu, G.; Hayton, T. W., Synthesis, Molecular and Electronic Structure of $U^V(O)[N(SiMe_3)_2]_3$. *Inorg. Chem.* **2012**, *51*, 1625-1633.
41. Bart, S. C.; Anthon, C.; Heinemann, F. W.; Bill, E.; Edelstein, N. M.; Meyer, K., Carbon Dioxide Activation with Sterically Pressured Mid- and High-Valent Uranium Complexes. *J. Am. Chem. Soc.* **2008**, *130*, 12536-12546.
42. Schmidt, A.-C.; Heinemann, F. W.; Maron, L.; Meyer, K., A Series of Uranium (IV, V, VI) Tritylimido Complexes, Their Molecular and Electronic Structures and Reactivity with CO_2. *Inorg. Chem.* **2014**, *53*, 13142-13153.
43. Mullane, K. C.; Lewis, A. J.; Yin, H.; Carroll, P. J.; Schelter, E. J., Anomalous One-Electron Processes in the Chemistry of Uranium Nitrogen Multiple Bonds. *Inorg. Chem.* **2014**, *53*, 9129-9139.
44. Mullane, K. C.; Carroll, P. J.; Schelter, E. J., Synthesis and Reduction of Uranium(V) Imido Complexes with Redox-Active Substituents. *Chem. Eur. J.* **2017**, *23*, 5748-5757.
45. Tsoureas, N.; Cloke, F. G. N., Mixed sandwich imido complexes of Uranium(V) and Uranium(IV): Synthesis, structure and redox behaviour. *J. Organomet. Chem.* **2018**, *857*, 25-33.
46. King, D. M.; Tuna, F.; McInnes, E. J. L.; McMaster, J.; Lewis, W.; Blake, A. J.; Liddle, S. T., Synthesis and Structure of a Terminal Uranium Nitride Complex. *Science* **2012**, *337*, 717-720.
47. Wilkerson, M. P.; Berg, J. M.; Hopkins, T. A.; Dewey, H. J., First observation of intra-5f fluorescence from an actinyl center: Np(VI) near-IR emission in $Cs_2U(Np)O_2Cl_4$. *J. Solid State Chem.* **2005**, *178*, 584-588.
48. Liu, G.; Wang, S.; Albrecht-Schmitt, T. E.; Wilkerson, M. P., Electronic Transitions and Vibronic Coupling in Neptunyl Compounds. *J. Phys. Chem. A* **2012**, *116*, 8297-8302.
49. Griffith, J. S., *The Theory of Transition-Metal Ions*. University Press: Cambridge, 1961.
50. Lever, A. B. P., *Inorganic Electronic Spectroscopy (second edition)*. Elsevier: New York, 1984.
51. Graves, C. R.; Yang, P.; Kozimor, S. A.; Vaughn, A. E.; Clark, D. L.; Conradson, S. D.; Schelter, E. J.; Scott, B. L.; Thompson, J. D.; Hay, P. J.; Morris, D. E.; Kiplinger, J. L., Organometallic Uranium(V)−Imido Halide Complexes: From Synthesis to Electronic Structure and Bonding. *J. Am. Chem. Soc.* **2008**, *130*, 5272-5285.
52. Kindra, D. R.; Evans, W. J., Magnetic Susceptibility of Uranium Complexes. *Chem. Rev.* **2014**, *114*, 8865-8882.
53. King, D. M.; Tuna, F.; McMaster, J.; Lewis, W.; Blake, A. J.; McInnes, E. J. L.; Liddle, S. T., Single-Molecule Magnetism in a Single-Ion Triamidoamine Uranium(V) Terminal Mono-Oxo Complex. *Angew. Chem. Int. Ed.* **2013**, *52*, 4921-4924.
54. Gendron, F.; Autschbach, J., Puzzling Lack of Temperature Dependence of the PuO_2 Magnetic Susceptibility Explained According to Ab Initio Wave Function Calculations. *J. Phys. Chem. Lett.* **2017**, *8*, 673-678.

55. Shick, A. B.; Kolorenč, J.; Havela, L.; Gouder, T.; Caciuffo, R., Nonmagnetic ground state of PuO_2. *Phys. Rev. B* **2014**, *89*, 041109.
56. Speldrich, M.; van Leusen, J.; Kögerler, P., CONDON 3.0: An Updated Software Package for Magnetochemical Analysis-All the Way to Polynuclear Actinide Complexes. *J. Comput. Chem.* **2018**, *39*, 2133-2145.
57. van Vleck, J. H., *The Theory of Electric and Magnetic Susceptibilities*. Oxford University Press: London, 1932.
58. Ryan, J. L., Halide complexes of pentavalent uranium. *J. Inorg. Nucl. Chem.* **1971**, *33*, 153-177.
59. Wilkerson, M. P.; Berg, J. M., Excitation spectra of near-infrared photoluminescence from Np(VI) in $Cs_2U(Np)O_2Cl_4$. *Radiochim. Acta* **2009**, *97*, 223-226.
60. Burdett, J. K., The σ strength of ligands coordinated to transition metal ions. *J. Am. Chem. Soc.* **1979**, *101*, 580-583.
61. The authors thank one of the Reviewers for making this observation.
62. Hansch, C.; Leo, A.; Taft, R. W., A survey of Hammett substituent constants and resonance and field parameters. *Chem. Rev.* **1991**, *91*, 165-195.
63. Edelstein, N. M.; Lukens, W. W., f-Orbital Mixing in the Octahedral f^2 Compounds UX_6^{2-} [X = F, Br, Cl, I] and $PrCl_6^{3-}$. *J. Phys. Chem. A* **2020**, *124*, 4253-4262.
64. Barros, N.; Maynau, D.; Maron, L.; Eisenstein, O.; Zi, G.; Andersen, R. A., Single but Stronger UO, Double but Weaker UNMe Bonds: The Tale Told by Cp_2UO and Cp_2UNR. *Organometallics* **2007**, *26*, 5059-5065.
65. Chatelain, L.; Walsh, J. P. S.; Pécaut, J.; Tuna, F.; Mazzanti, M., Self-Assembly of a 3d–5f Trinuclear Single-Molecule Magnet from a Pentavalent Uranyl Complex. *Angew. Chem. Int. Ed.* **2014**, *53*, 13434-13438.
66. Andersen, R. A., Tris((hexamethyldisilyl)amido)uranium(III): preparation and coordination chemistry. *Inorg. Chem.* **1979**, *18*, 1507-1509.
67. Bain, G. A.; Berry, J. F., Diamagnetic Corrections and Pascal's Constants. *J. Chem. Ed.* **2008**, *85*, 532.
68. *SMART Apex II, Version 2.1 ed.; Bruker AXS Inc.: Madison WI*, 2005.
69. *SAINT Software User's Guide, Version 7.34a ed.; Bruker AXS Inc.: Madison, WI*, 2005.
70. Sheldrick, G. M. *SADABS, the Siemens Area Detector Absorption Correction; University of Göttingen: Göttingen, Germany*, 2005.
71. *SHELXTL PC, Version 6.12 ed.; Bruker AXS Inc.:Madison, WI*, 2005.

TOC Graphic

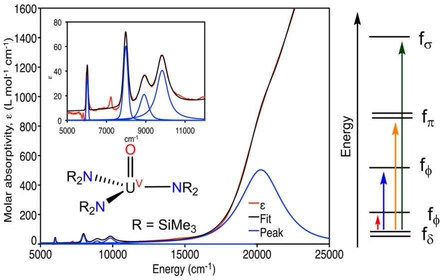

Summary: The f_δ ground state of the U(V) oxo complex, $[U^V(NR_2)_3(O)]$ (R = $SiMe_3$), is determined primarily by the O-U-N_{amide} angles.